PLANETARY SCIENCE

Widespread hematite at high latitudes of the Moon

Shuai Li[1]*, Paul G. Lucey[1], Abigail A. Fraeman[2], Andrew R. Poppe[3], Vivian Z. Sun[2], Dana M. Hurley[4], Peter H. Schultz[5]

Copyright © 2020 The Authors, some rights reserved; exclusive licensee American Association for the Advancement of Science. No claim to original U.S. Government Works. Distributed under a Creative Commons Attribution NonCommercial License 4.0 (CC BY-NC).

Hematite (Fe_2O_3) is a common oxidization product on Earth, Mars, and some asteroids. Although oxidizing processes have been speculated to operate on the lunar surface and form ferric iron–bearing minerals, unambiguous detections of ferric minerals forming under highly reducing conditions on the Moon have remained elusive. Our analyses of the Moon Mineralogy Mapper data show that hematite, a ferric mineral, is present at high latitudes on the Moon, mostly associated with east- and equator-facing sides of topographic highs, and is more prevalent on the nearside than the farside. Oxygen delivered from Earth's upper atmosphere could be the major oxidant that forms lunar hematite. Hematite at craters of different ages may have preserved the oxygen isotopes of Earth's atmosphere in the past billions of years. Future oxygen isotope measurements can test our hypothesis and may help reveal the evolution of Earth's atmosphere.

INTRODUCTION

The lunar surface and interior are highly reducing [e.g., (*1*)]. Metallic iron is found as a primary igneous phase in lunar basalts and ferric iron (Fe^{3+}) is virtually absent (*1*). The lack of atmosphere on the Moon allows solar wind (most of which is H) to reach the lunar surface and be implanted into the top tens to hundreds of nanometers of layer of surface grains, which would reduce any ferric iron to lower valence or even metallic iron during impact events (*2*). Iron in Apollo samples is dominantly ferrous (Fe^{2+}) or metallic, and the upper limit of ferric iron–bearing materials is less than 1 weight % (wt %) [e.g., (*3*)], which reflects the highly reduced state of the Moon.

Despite the reducing environment, ferric iron–bearing minerals have been theorized to form on the lunar surface (*4*–*6*). The recognition that the lunar poles harbor water ice led to studies regarding the possibility of alteration due to minerals in contact with ice (*4*) or vapor from sublimating ice (*5*). In addition, a recent study shows that plasmas sourced from Earth's upper atmosphere (so called "Earth wind") may have delivered a substantial amount of oxygen to the lunar surface in the past 2.4 billion years during the passage of the Moon through Earth's magnetotail (*7*). This terrestrial oxygen could naturally oxidize lunar surface low-valence iron to ferric iron.

Discovering and mapping any ferric iron–bearing minerals on the lunar surface would reveal if oxidation is occurring under highly reducing conditions and may help shed light on processes that form oxidation products on other airless bodies. For instance, the presence of ferric iron, along with phyllosilicate on asteroids, is commonly attributed to aqueous alteration [e.g., (*8*)]. while the formation of ferric iron that is not associated with phyllosilicate on asteroids is enigmatic (*8*, *9*). However, the detection of ferric iron–bearing species on the Moon has remained elusive in sample analyses and remote observations. Ferric iron–bearing minerals FeOOH (goethite, lepidocrocite, and akaganeite), Fe_2O_3 (hematite and maghemite), and Fe_3O_4 (magnetite) were found in some Apollo samples [e.g., (*3*, *10*, *11*, *12*)], but some of these studies argued that those alteration phases were products of possible terrestrial contamination [e.g., (*10*)]. The Solid State Imager (SSI) onboard the Galileo mission detected a possible ferric absorption near 0.7 μm at high latitudes of the Moon (>58°S) during its flyby, but that study could not determine whether that absorption was caused by phyllosilicates, ilmenite, ferric iron–bearing clinopyroxene, or other species (*13*).

Hematite is an excellent ferric target for remote detection using visible, near-infrared (VNIR) spectroscopy because of its unique spectral properties relative to common lunar materials (fig. S1). In particular, the absorption centered near 0.85 μm of hematite due to the $^4T_1 \leftarrow {}^6A_1$ charge transfer between Fe^{3+} and O^{2-} is not shared by any common lunar mineral or other ferric oxides. In contrast, the three forms of FeOOH (goethite, akaganeite, and lepidocrocite) and maghemite (γ-Fe_2O_3) all have absorptions near 0.95 μm that overlap with absorptions of pyroxene, which complicates their detections, while magnetite (Fe_3O_4) spectra are dark and featureless (fig. S1).

The Moon Mineralogy Mapper (M^3) onboard the Indian Chandrayaan-1 mission was a VNIR imaging spectrometer that collected reflectance data between 0.46 and 2.98 μm at spectral resolutions of 20 to 40 nm and spatial resolution samplings of 140 to 280 m per pixel in global mapping mode (*14*). Global surface maps created in this mode allow us to search for hematite that contains ferric iron across the lunar surface. M^3 data are thermally corrected using the model of (*15*). However, since the relevant wavelengths needed to identify hematite are all shorter than 1.2 μm, thermal corrections have no effect on our detections. Laboratory spectra of hematite have a diagnostic absorption near 0.85 μm that starts at around 0.75 μm and ends at around 1.2 μm, and an additional absorption near 0.66 μm (Fig. 1). Hematite also has a diagnostic absorption at around 0.53 μm (*16*), but the first two spectral channels (0.46 and 0.50 μm) of the global mode M^3 dataset are not well calibrated (*14*), so this absorption cannot be definitively identified. We search for candidate hematite absorptions in M^3 data by calculating the absorption depths of all bands between 0.75 and 1.2 μm [referred to as the integrated band depth (IBD) of the 0.85-μm absorption] and indicate that pixels with high IBD values may contain hematite (see Materials and Methods).

RESULTS

Our global search for hematite revealed that hematite-like absorptions near 0.85 μm are widespread at high latitudes of the Moon.

[1]Hawai'i Institute of Geophysics and Planetology, University of Hawaii, Honolulu, HI 96822, USA. [2]Jet Propulsion Laboratory, California Institute of Technology, Pasadena, CA 91109, USA. [3]Space Sciences Laboratory, University of California at Berkeley, Berkeley, CA 94720, USA. [4]Applied Physics Laboratory Johns Hopkins, Laurel, MD 20723, USA. [5]Department of Earth, Environmental and Planetary Sciences, Brown University, Providence, RI 02912, USA.
*Corresponding author. Email: shuaili@hawaii.edu, njushuaili@gmail.com

Downloaded from http://advances.sciencemag.org/ on September 14, 2020

Figure 1 shows two M^3 spectra of putative hematite–rich pixels compared with laboratory hematite. The M^3 spectra exhibit a pair of absorptions near 0.85 and 0.66 μm consistent with those of hematite (Fig. 1B and Table 1), which strongly suggests that the two M^3 pixels are rich in hematite. The hematite absorption near 0.53 μm could not be verified because of uncertain calibration of the global mode M^3 data shortward of 0.54 μm (*14*) and no target mode M^3 observations at high latitudes (>60°) (*17*). The weaker absorptions at 0.85 and 0.66 μm in M^3 data compared with laboratory hematite spectra could be due to space weathering that can weaken absorptions (*18*) or differences in hematite particle size and abundance [e.g., (*16*, *19*)]. However, there is lack of studies to show how space weathering can affect the absorption of ferric iron–bearing minerals (i.e., hematite). The 0.66-μm absorption seen in M^3 data might be the one centered near the 0.7-μm channel that was observed in the SSI data (*13*).

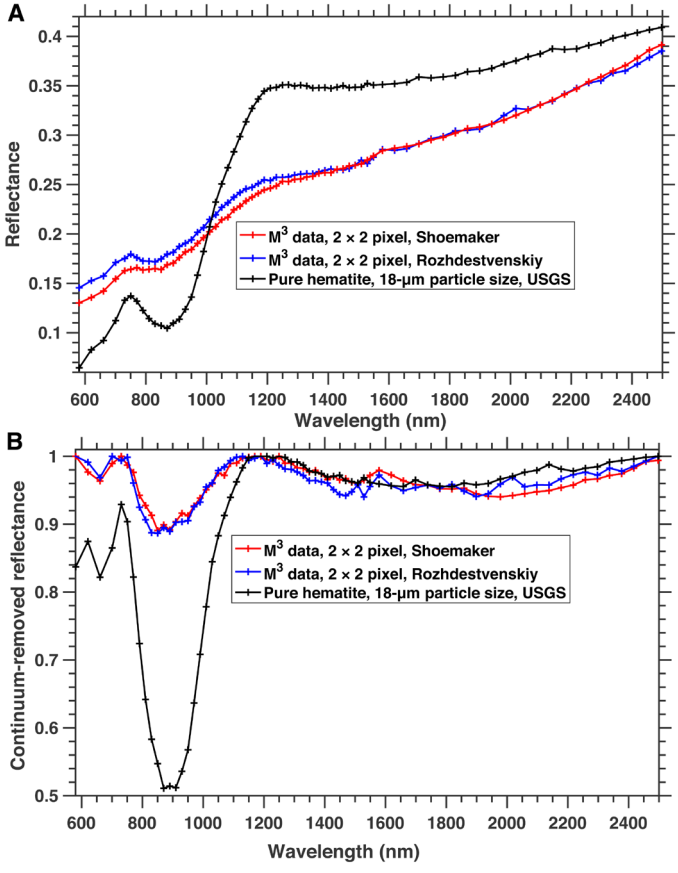

Fig. 1. Examples of M^3 spectra at hematite-rich pixels. The hematite-rich M^3 spectra are compared with laboratory spectra of pure hematite (**A**) and comparison after continuum removal (**B**).

We do not see promising spectral features of other alteration minerals such as goethite, maghemite, and magnetite, to name a few. Either they are not present on lunar surface because of the low oxygen fugacity [hematite will be preferentially formed under low oxygen (*20*)] or their detections are complicated by the spectral absorptions of typical lunar surface minerals (e.g., pyroxene) (fig. S1) or hematite (*21*).

Three key features of hematite distribution are observed in our global mapping of hematite. First, it shows that almost all putative hematite detections are at latitudes above 60° in both hemispheres (fig. S2). Figure 2 shows the maps of the IBD values near 0.85 μm at the northern and southern polar regions from 75° to 90° overlain on the maps of all examined M^3 pixels (see Materials and Methods). The IBDs of the 0.85-μm absorption exhibit very weak latitudinal dependence from 75° to the poles (fig. S3). Pixels with similar IDBs are interpreted to the presence of similar amount of hematite (see Materials and Methods). Second, the density plots of azimuth angles of hematite exposures in the northern and southern polar regions suggest that hematite-rich pixels are more abundant at the east- and equator-facing sides of topographic highs (Fig. 3), and occurrences on flat surfaces such as crater floors are rare (Fig. 2). The east-west asymmetry of hematite exposures is less evident on the lunar farside than the nearside, particularly at the northern polar region (Fig. 3A). Third, the lunar nearside shows more hematite-rich pixels than the farside of the Moon (Figs. 2 and 3). The M^3 coverage is similar on the nearside and farside of the Moon (Fig. 2). In addition, the density plots of hematite exposures in Fig. 3 are normalized by the number of examined M^3 pixels and still show that hematite is more concentrated on the nearside of the Moon. These plots all suggest that the hematite distribution is real and not an artifact of data coverage and may be a clue to its formation processes.

The absorption strength of our detected hematite-bearing pixels near 850 nm exhibits no dependence on surface roughness and reflectance albedo at 1489 nm (fig. S4). There seems to be a very weak positive correlation between the 850-nm band depth and phase angles (fig. S5, A and C). We attribute this weak correlation to the latitudinal dependence of the 850-nm absorption strength (fig. S3). A much less reducing and relatively water-richer environment at higher latitudes

Table 1. Observed and modeled band centers and full width at half maximum (FWHM) values of the absorption near 850 nm. The spectral resolution of M^3 data at the spectral range of 700 to 1529 nm is 20 nm. N/A, not applicable; USGS, U.S. Geological Survey.

Spectra	Observed 850-nm absorption		Modeled 850-nm absorption					
			Coarse hematite		Fine hematite		No hematite	
	Center*	FWHM	Center	FWHM	Center	FWHM	Center	FWHM
Rozhdestvenskiy	850	200	870	190	870	180	920	190
Shoemaker	850	200	N/A		N/A		N/A	
USGS hematite	870	200	N/A		N/A		N/A	

*Band centers are determined as the absorption peaks after continuum removal (Figs. 1B and 4); the units of absorption centers and FWHM are nanometer.

Downloaded from http://advances.sciencemag.org/ on September 14, 2020

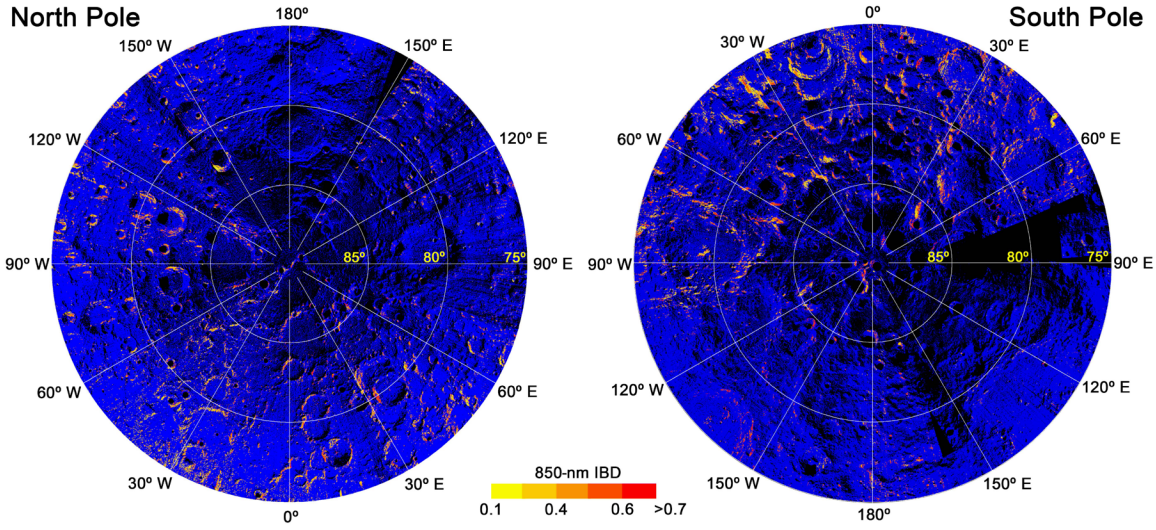

Fig. 2. The IBD near 0.85 μm at the northern and southern polar regions from 75° to 90°. The 0.85-μm IBD used as an indicator for the presence of hematite is overlain on the maps of all examined M^3 pixels (blue) at both poles; black regions indicate a lack of high-quality M^3 data (see Materials and Methods).

may fertilize more hematite formation and retention than lower latitudes. More water is observed at higher latitudes and also, the solar wind flux (rich in hydrogen, the reductant agency) decreases with increasing latitudes (fig. S2). For instance, the hydrogen fluxes at 75° and 85° latitudes on the lunar surface are approximately 26% (cos75°) and 9% (cos85°) of that at the equator, respectively, which suggests a much less reducing environment at lunar high latitudes. We also find that there is no shift in phase angles between our examined M^3 pixels and those hematite detections (fig. S5, B and D). We examined the M^3 data of the same location (e.g., the Rozhdestvenskiy crater) acquired at different optical periods (OPs) and found almost identical hematite-like absorption features between those two OPs (fig. S6). All these suggest that our detections of hematite are not affected by the surface roughness, albedo, observation geometry, and observation time.

The Hapke's radiative transfer model (*22*) is applied to perform spectral unmixing to estimate the abundance of hematite. Given the fact that the IBDs at 850 nm exhibit very weak latitudinal dependence across the polar regions (fig. S3), we can use the M^3 spectra of hematite-bearing pixels at Rozhdestvenskiy (Fig. 4) to represent the hematite exposures in the lunar polar regions because their IBD values at 850 nm are similar to the mean value of the northern and southern polar regions (~0.5, fig. S3). Assuming intimate mixing with lunar regolith, we fit the M^3 data with and without the hematite end-member. We assume that hematite has the same particle size as other end-members or that the particle size of hematite could be much finer than the regolith (see Materials and Methods). We also test a third scenario that a nanophase hematite (<1 μm) is embedded in the top tens to hundreds of nanometers of layer of grains as coatings. Coating effects are incorporated into our implementation of the Hapke's model (see Materials and Methods). Fits of the 0.85-μm band of lunar data are excellent with hematite included as an end-member, while fits are poor near 0.85 μm without the hematite end-member (Fig. 4 and Table 1). The curve fitting results at longer wavelengths are available in fig. S7. The band centers of M^3 spectra and modeled spectra with and without the hematite end-member are at 850, 870, and 920 nm, respectively (Table 1), which strongly suggest the presence of hematite in the two M^3 spectra. The full width at half maximum (FWHM) values of M^3 and U.S. Geological Survey (USGS) pure hematite spectra are 200 nm. While the modeled spectra show slightly smaller FWHM values at 180 and 190 nm for the fine and coarse hematite scenarios, respectively. The difference of FWHM between observed and modeled spectra is no more than one M^3 spectral band (20 nm from 700 to 1529 nm). The spectral unmixing results show that if the hematite and regolith have a similar particle size, 10 to 20 μm as suggested in (*18*), then ~11 wt % hematite is required to reproduce the absorption feature seen in M^3 data (Fig. 4), while if the hematite has a much finer particle size (i.e., 1 to 10 μm), then ~4 wt % of fine hematite can fit the M^3 absorption very well (Fig. 4). However, the model cannot fit the M^3 data well by assuming nanophase hematite coating (fig. S8), which suggests that the hematite seen on the lunar surface is most probably micron sized or larger and its abundance may range from a few weight % to around 10 wt %.

DISCUSSION

We propose a model where oxygen from Earth wind, water in lunar regolith, and heat induced by interplanetary dust impact provide an environment for lunar regolith to oxidize to form hematite or undergo oxyhydration to form FeOOH that is dehydrated to hematite. The formed hematite can be reduced by solar wind hydrogen. The hematite distribution on the lunar surface should be controlled by the trade-off between the oxidization/oxyhydration processes, under the presence of oxygen, iron, water, and interplanetary dust impacts, and the reduction processes by solar wind hydrogen. Oxygen can oxidize low-valence iron (e.g., Fe^{2+} and Fe^0) in lunar regolith to form hematite and FeOOH with and without the presence of molecular water, respectively (see the Supplementary Materials). Strong hydration features are observed at high latitudes of the Moon, most of which could be hydroxyl and enriched in rims of lunar surface grains [e.g., (*23*–*25*)]. Molecular water is theorized to form from hydroxyl during impact events (*26*) and hypervelocity impact experiments reveal that molecular water can be delivered, generated, and trapped during impact events (*27*). The molecular water may react with submicroscopic iron metal in rims of lunar grains to form FeOOH (*28*). It can also liberate Fe^{2+} to increase the reaction rates of the oxidation and oxyhydration processes. Heat induced by interplanetary dust impact

Downloaded from http://advances.sciencemag.org/ on September 14, 2020

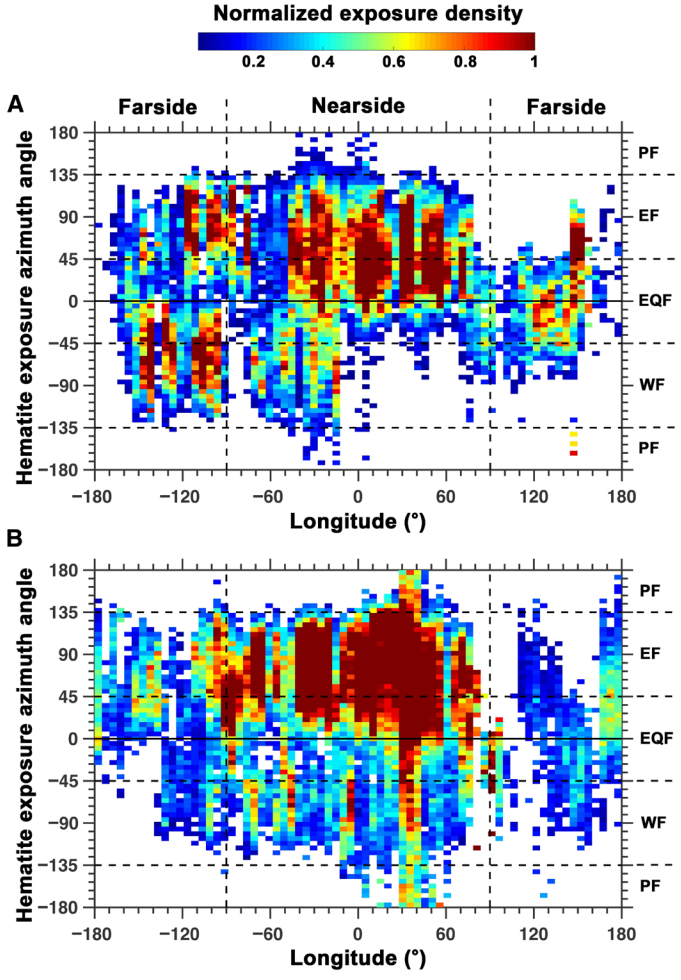

Fig. 3. Density plots of azimuth angles of hematite exposures at each longitude zone in the polar regions. The azimuth angles of hematite exposures are binned with a 5° longitude window from 75° to 90° latitudes [(**A**) North Pole and (**B**) South Pole], normalized by the number of examined M^3 pixels in each bin, and then stretched 2% linearly from 0 to 1; PF, pole facing; EF, east facing; WF, west facing; EQF, equator facing.

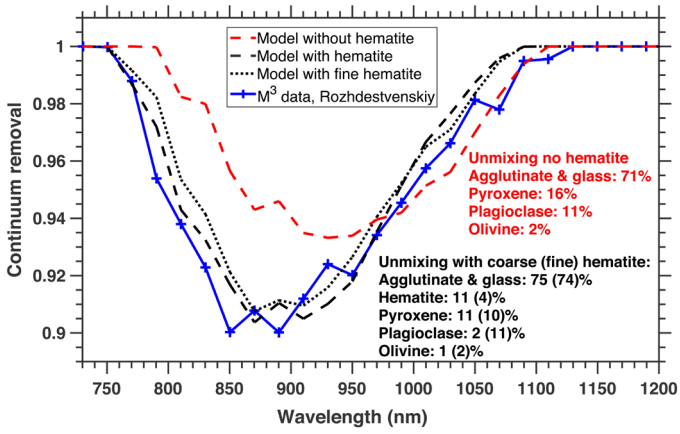

Fig. 4. Spectral unmixing results of M^3 data at hematite exposures using the Hapke's radiative transfer model at the Rozhdestvenskiy crater. The curve fitting near 0.85 μm is substantially improved after including both coarse and fine grain hematite end-members.

may have played critical roles in liberating molecular water and enhancing the reaction processes to form hematite and FeOOH (see the Supplementary Materials). Although FeOOH is suggested to be thermally stable over geologic time in the polar regions (*4*), it can be decomposed to hematite by solar radiation, impact, and sputtering (*5*, *10*, *28*). The hydrogen flux from solar wind at the equator is several times higher than that in the polar regions (fig. S2). More hematite can be reduced at lower latitudes than higher latitudes.

Any successful hypothesis for the hematite formation on the Moon should be able to explain its spatial distribution. The dichotomous distribution of hematite between the nearside and farside of the Moon can be attributed to the fact that oxygen from Earth wind (*7*) mostly reaches the nearside of the Moon (*29*). Observations from the Japanese Kaguya mission found that 2.6×10^4 cm^{-2} s^{-1} O^+ can be delivered to the lunar nearside surface by plasma sourced from Earth's upper atmosphere (Earth wind) and implanted into the lunar regolith (*7*). Our calculation suggests that such oxygen is sufficient to form around 5 to 9 wt % hematite (see the Supplementary Materials), which is adequate to explain the amount of hematite mapped on the Moon (Figs. 2 and 4). Although the oxygen flux is even higher in the solar wind (*30*) than that from Earth wind, hydrogen, the dominant species in solar wind, makes the lunar surface environment highly reducing. However, when the Moon is in Earth's magnetotail, the solar wind flux can be reduced to less than 1% of that out of the magnetotail (*31*). Observations suggest that the oxygen density in terrestrial plasmas (Earth wind) in the magnetotail can be even higher than hydrogen density during magnetic storms (e.g., *32*). In addition, neutral oxygen is continuously liberated from the surface of the Moon via processes such as micrometeoroid bombardment and charged-particle sputtering [e.g., (*33*)] and has been detected in both its neutral and ionized states [e.g., (*34*)]. A previous study by Poppe *et al.* (*35*) has shown that approximately one-third of the oxygen atoms ejected into the lunar exosphere will be recycled back into the soil as they are ionized (by either photoionization, charge exchange, or electron impact ionization) and accelerated by ambient electric fields (arising from either solar wind or magnetotail convection). As shown in the Kaguya observations by Terada *et al.* (*7*), the lunar exospheric oxygen ion fluxes can be equal to or larger than ions sourced from terrestrial ionospheric outflow. However, the implantation depth of the lunar exospheric oxygen could be much smaller than that of the Earth's wind oxygen due to a much lower energy of the former (*7*), which may substantial suppress the oxidization and oxyhydration processes. This could explain the lack of hematite exposures in regions on the lunar farside (Figs. 2 and 3), where lunar exospheric oxygen might be similar to that on the nearside. In summary, low hydrogen flux and oxygen mostly from Earth wind make the lunar nearside surface relatively oxidizing when the Moon is in Earth's magnetotail, while the lunar farside receives no/little terrestrial oxygen because it faces away from the Earth.

It is noteworthy that hematite is not absolutely absent on the lunar farside (Figs. 2 and 3). There, a small amount of FeOOH might be formed under the presence of water and energies induced by interplanetary dust impacts and then be decomposed to hematite, similar to the pathway in (*28*). Alternatively, a small amount of Earth's wind oxygen might be available in regions not deep into the farside to from hematite or FeOOH, depending on the presence of

Downloaded from http://advances.sciencemag.org/ on September 14, 2020

molecular water (see the Supplementary Materials) (Figs. 2 and 3, particularly in the northern polar region). However, high fluxes of solar wind hydrogen at low latitudes may have reduced all formed hematite.

The correlation between hematite detections and high latitudes suggests that enriched hydration at high latitude (*23*–*25*, *36*, *37*) may have played an important role in hematite formation. Molecular water associated with impact events (see the Supplementary Materials) may have helped to liberate Fe^{2+}, which can increase the reaction rate of Fe^{2+} and oxygen to form hematite (see the Supplementary Materials). More hematite exposures are observed at higher latitudes where there is also more hydration (fig. S2) (*23*–*25*, *36*, *37*). Similarly, the lack of hematite detections at low latitudes may be attributed to a much lower hydration and higher solar wind fluxes at latitudes less than around 60° in both hemispheres (fig. S2). Although a sharp increase of water contents is observed at latitudes from 60° to 75° (fig. S2), the solar wind hydrogen flux may be still high enough to reduce most of the hematite formed at this latitude zone on both hemispheres.

Highly concentrated hematite exposures at east- and equator-facing sides of topographic highs might be associated with interplanetary dust impacts. The impact may have played two roles. First, the impact heat can increase the reaction rate of oxidization and oxyhydration. Second, impacts can deliver, generate, and trap molecular water (*26*, *27*). Molecular water and impacts (*38*) can liberate Fe^{2+} to form hematite. The ideal scenario for hematite formation could be the simultaneous presence of Earth's wind oxygen and Fe^{2+} liberated by molecular water during impact events. Our simulations suggest that the east- and equator-facing sides of topographic highs may receive much more "effective" interplanetary dust impacts than other facing sides (fig. S9). An effective impact is defined as that an interplanetary dust impact on a surface bathed in Earth's wind oxygen, which helps to liberate Fe^{2+} into Earth's wind oxygen to boost the hematite formation. In contrast, interplanetary dusts affecting on shaded surfaces are not considered as effective impacts because of the lack of Earth's wind oxygen (the oxidant). The simulations are done for high latitudes (e.g., 80°) because only the polar regions exhibit an enhanced hydration for hematite formation and a much lower solar wind hydrogen flux to reduce hematite (fig. S2), while there may be no Earth's wind oxygen available on the lunar farside, and thus, no need to discriminate whether an impact is on a shaded or illuminated surface. In such a case, our simulations suggest almost no difference between the east- and west-facing slopes on the lunar far-side (fig. S9). This may explain the less asymmetric distribution of hematite exposures on east- and west-facing slopes on the lunar farside, particularly in the northern polar region (Fig. 3A).

The hematite absorption strength shows very weak latitudinal dependence (fig. S3), which suggests that the hematite content might be similar at each latitude from 75° to the pole if the mapped hematite shows similar particle size and optical maturity (see Materials and Methods). In our model, the amount of hematite that can be formed at each exposure is controlled by the availability of iron, water, oxygen, and energy sources. The deformation of hematite may be mostly controlled by the reducing process of solar wind hydrogen. The iron content in the polar regions is quite homogenous (*39*). The water content is higher at higher latitudes (fig. S2), which may fertilize more hematite formed. Modeling results suggest that the flux of interplanetary dust impacts decreases as latitudes increase (*40*), which indicates that less energy is available for hematite formation at higher latitudes. However, the solar wind flux drops at higher latitudes, which suggests a less reducing environment at higher latitudes and thus higher chance for hematite to be preserved. The current biggest unknown is how the oxygen flux from Earth wind varies with the latitude on the lunar surface. Future investigations are needed to understand which of the above factor(s) controls the amount of hematite that can be formed and retained.

It is unclear why crater floors and other relatively flat surfaces show much less hematite exposures than tilted surfaces (Fig. 2). One possible explanation is that hematite may also form on flat surfaces but it might have been reduced to ferrous or metallic iron by solar wind hydrogen. The daily solar wind influence on steep surfaces (i.e., crater walls and central peaks) can be much lower than that of flat surfaces due to the shadow effect, and thus, much more hematite on steep surfaces might have been preserved.

The presence of hematite on some S-type (*9*) and low albedo (*8*) asteroids not associated with aqueous alteration may not need the presence of oxygen. Interplanetary dust impact (*41*), solar wind–induced hydration [e.g., (*23*, *24*, *25*)], and submicroscopic iron metal [e.g., (*42*)] are also suggested on these airless bodies. A small amount of FeOOH might be formed first under the presence of iron metal, water, and impact energy, while FeOOH was then decomposed to hematite, as suggested to possibly operate on the lunar farside in this study and in (*28*). Although similar conditions also operate at the lunar low latitudes, the rate of reduction by solar wind hydrogen could be much higher than that at high latitudes (i.e., >75°), and thus, little hematite may have been preserved at lunar low latitudes (fig. S2 and the Supplementary Materials).

The band center of the absorption near 850 nm may help reveal the purity of hematite crystals on the lunar surface. The substitution of Al^{3+} for Fe^{3+} in hematite is commonly found in natural samples [e.g., (*43*)]. Previous studies suggest that Al^{3+} substitutions in hematite can shift the band center from ~850 to 900 nm with 0 and ~60 mole % substitution, respectively (*44*). In our observations, the band center of hematite-bearing pixels is around 850 nm, which may suggest that the hematite on the lunar surface has no or very little Al substitutions. However, using the band center of the absorption near 850 nm may result in large uncertainty in estimating the Al substitution due to the low spectral resolution of M^3 data (20 nm at the range of 700 to 1529 nm). In addition, it is still unclear how the particle size and other cation substitutions (e.g., Ni^{2+}, Cr^{3+}, Mn^{3+}, and Ti^{4+}) can affect the absorption center of hematite near 850 nm [e.g., (*43*, *44*)].

Future oxygen isotope measurements at hematite exposures, particularly on the lunar nearside, can help test our hypotheses about hematite formation. If hematite is oxidized from low-valence iron by oxygen from Earth's upper atmosphere, then its isotope should resemble that of Earth's upper atmosphere, poor in ^{16}O [e.g., (*45*)]. Hematite formed at craters of different ages on the lunar nearside may record the oxygen signatures of Earth's atmosphere in the past ~2.4 billion years. Isotope measurements at these hematite exposures can reveal the evolution of Earth's atmosphere in the past billions of years. It is suggested that the lunar polar regions are relatively iron poor (*39*). Thus, our mapped hematite can be important in situ resources for iron metal.

Two diagnostic absorptions near 0.85 and 0.66 μm are seen in M^3 data that are consistent with the presence of hematite. Little to no hematite is detected at latitudes less than around 60° in both hemispheres. The strength (IBD) of the 0.85-μm absorption, a proxy of hematite content, shows very weak latitudinal dependence from 75° to the poles. Spectral unmixing results suggest a few to around

Downloaded from http://advances.sciencemag.org/ on September 14, 2020

10 wt % hematite on the lunar surface. Hematite exposures are mostly located at the east- and equator-facing sides of topographic highs, such as the western crater walls and eastern sides of central peaks. There is a dichotomy in the distribution of hematite between the nearside and farside of the Moon with more exposures on the nearside, particularly in the southern polar region. We hypothesize that hematite formation on the Moon may involve oxidization/oxyhydration processes, and its distribution may be controlled by the availability of iron, water, energy induced by interplanetary impact, and oxygen from Earth's upper atmosphere and lunar exosphere. Our hypothesis may be also applicable to some airless bodies where hematite formation is not associated with phyllosilicate, possibly similar to the hematite formation on the lunar farside where FeOOH can be formed first and then be decomposed to hematite. Future oxygen isotope measurements at hematite exposures can help test our hypothesis. Studying the oxygen isotopes of hematite at different age craters may help reveal the evolution of Earth's atmosphere in the past billions of years. Our mapped hematite can be important in situ resources for iron metal in the iron-poor polar regions.

MATERIALS AND METHODS

M^3 data are used to detect hematite across the global lunar surface. The M^3 L1B radiance data were downloaded from the NASA Planetary Data System (PDS) server and then converted to reflectance, with the same method used in (*15*). We perform a series of processes to convert radiance to photometrically corrected reflectance. These processes are converting radiance to IoF, statistical polishing, thermal removal, and photometric correction. The solar distance of M^3 data are considered in the calculation of IoF (*17*). The statistical polishing factors (radiance correction factors) are available in the PDS release of M^3 level 2 data (*17*). We used our newly developed thermal model to remove the thermal effects of M^3 data (*15*). The photometric correction is performed in the same way as that in (*46*). The detailed description of each correction can be found in (*17*) and (*15*).

The signal-to-noise ratio (SNR) of M^3 data at high latitudes is downgraded because of high phases and shadows (*14*). Low-SNR M^3 data (high noise level) are masked to ensure robust detections of hematite-like absorption near 0.85 μm. Mathematically, the integral of squared second derivatives (ISSD) of a curve is commonly used to assess the smoothness (noise level) of that curve. Part of the M^3 data at the polar regions is affected by shadows and high phases and exhibits low SNRs. The water bands near 3 μm of M^3 data show a strong variation at the polar regions (*37*), which may affect the assessment of the noise level of M^3 spectra. We only use the spectral bands between 0.58 and 2.5 μm to calculate the ISSD and use it as an indicator for the noise level of M^3 spectra. We find that a threshold of ISSD greater than 0.05 can mask most of the M^3 pixels showing "strip" noise (column-dependent noise) and pixels affected by shadows. Only around 10% of M^3 pixels have ISSD values greater than 0.05 (fig. S10). We color the M^3 pixels with ISSD less than 0.05 as blue and ISSD greater than 0.05 as black to indicate low-SNR pixels not examined in Fig. 2.

The IBD of the 0.85-μm absorption is used to search for hematite in conjunction with M^3 data. Laboratory spectra of hematite exhibit a unique absorption centered near 0.85 μm due to the $^4T_1 \leftarrow {}^6A_1$ charge transfer between Fe^{3+} and O^{2-}. The left shoulder of this absorption centers near 0.75 μm, while the right shoulder is near 1.2 μm (fig. S1). Thus, the strength of the 0.85-μm absorption can be used as a proxy for the hematite content if the particle size of lunar surface hematite is similar as typical lunar regolith whose optical properties are controlled by particles 10 to 20 μm in size (*18*). We convert all M^3 reflectance spectra to single scattering albedo (SSA) using the Hapke's model to minimize the effects from multiple scattering and albedo variation (*22*). We then chose two tie points at 0.75 and 1.2 μm to perform a continuum removal for all M^3 SSA. If an M^3 SSA spectrum after continuum removal shows an absorption at the region of 0.75 to 1.2 μm and also exhibits an absorption minimum at 0.85 μm, then it may indicate the presence of hematite and the absorption depths of all M^3 bands between 0.75 and 1.2 μm are summed (this is defined as IBD) as a proxy for the hematite content (fig. S11). We also compare the M^3 spectra at hematite-rich regions with the laboratory spectra of pure hematite to validate our detections. In addition to the minimum near 0.85 μm, we find that the spectra also have a reflection maximum near 0.75 μm and another minimum near 0.66 μm, consistent with hematite (Fig. 1). Nanophase metallic iron in mature lunar soil can substantially reduce the absorption strength (*18*). Therefore, the IBD of the 0.85-μm absorption can only indicate the relative hematite content of lunar regolith with similar maturity and may not be able to represent the absolute content of hematite. A more sophisticated approach is needed to quantify the absolute content of hematite on the lunar surface by taking into account of the effect of space weathering.

The Hapke's radiative transfer model is used to quantify the absolute hematite abundance. In the Hapke's model, a reflectance spectrum, R, can be described as a function of SSA, ω, and viewing geometry (i, e, and g). The SSA itself is a function of the optical constants $n(\lambda)$ and $k(\lambda)$ and is also dependent on the optical path length, $\langle D \rangle$, which can be related to particle size, D. The relationship between reflectance and these parameters can be expressed as (*22*)

$$R = \frac{\omega_{ave}}{4\pi}\frac{\mu_0}{\mu_0+\mu}\{[1+B(g,\phi)]P(g)+H(\mu_0,\omega_{ave})H(\mu,\omega_{ave})-1\} \quad (1)$$

Here, ω_{ave} is the average single scattering of all end-members weighted by particle size d and density ρ, μ_0 is the cosine of the incidence angle, μ is the cosine of emergence angle, ϕ is the porosity, $B(g, \phi)$ accounts for the opposition effect, $P(g)$ is the phase function, and H is the multiple scattering function. We set $\omega_{ave} = \Sigma_i M_i \omega_i$, where M represents the fractional extinction coefficient for each end-member (*22*). These fractional values can be converted to mass or volume fractions if the density and particle size for each mineral end-member is known (*22*). The detailed parameterizations for ω, μ, μ_0, $B(g, \phi)$, $P(g)$, and the H functions used in this study are the same as that of Li and Li (*47*) and Li and Milliken (*48*). The shape of particles in the Hapke's model is assumed as to be spherical (*22*). We have adopted a new relationship between the optical path length $\langle D \rangle$ and the particle size D: $\langle D \rangle = 0.2D$ (*49*) in our model implementation to accommodate the effect from the irregular shape of particles.

End-member spectra of typical lunar surface minerals for estimating hematite content are from Apollo and Luna separates and are plotted in fig. S1B. The spectrum of hematite end-member is from the USGS spectral library. The physical properties of our end-members are listed in table S1. The optical constants (n and k) of all end-members are derived using Eq. 1 from their reflectance spectra of pure phases, which is the same as (*47*). Derived optical constants and densities in table S1 of all end-member and reflectance spectra of hematite-rich pixels are then inserted into Eq. 1 to solve the mass fraction and particle size

Downloaded from http://advances.sciencemag.org/ on September 14, 2020

as free parameters (*48*, *50*). The curve fitting residuals are also output by our model. We test three different scenarios. First, we set the particle size of hematite the same as the rest end-members at 10 to 20 μm (the mean value of 15 μm is used) that is suggested in Apollo samples (*18*) and has been be also used by other studies [e.g., (*51*)]. Then, we restrict the particle size of the hematite end-member to be between 1 and 10 μm for the fine hematite scenario. We also test a third scenario assuming nanophase hematite (<1 μm) embedded in the top tens to hundreds of nanometers of layer of surface grains [(*52*) and references therein] by updating the absorption coefficient (α) in Eq. 1 (*2*)

$$\alpha = \frac{4\pi n_h k_h}{\lambda} + \frac{36\pi z M_{\mathrm{Hm}} \rho_h}{\lambda \rho_{\mathrm{Hm}}} \quad (2)$$

where n_h, k_h, and ρ_h are refraction indices, absorption coefficients, and densities of host materials, respectively; similarly, n_{Hm}, k_{Hm}, and ρ_{Hm} are refraction indices, absorption coefficients, and densities of hematite, respectively; λ is wavelength; M_{Hm} is the mass fraction of hematite; z is expressed as

$$z = \frac{n_h^3 n_{\mathrm{Hm}} k_{\mathrm{Hm}}}{\left(n_{\mathrm{Hm}}^2 - K_{\mathrm{Hm}}^2 + 2 n_h^2\right)^2 + 4 n_{\mathrm{Hm}}^2 k_{\mathrm{Hm}}^2} \quad (3)$$

The detailed parameterization of the Hapke's model for accommodating the coating effects is the same as that of (*47*).

SUPPLEMENTARY MATERIALS

Supplementary material for this article is available at http://advances.sciencemag.org/cgi/content/full/6/36/eaba1940/DC1

REFERENCES AND NOTES

1. G. J. Taylor, P. Warren, G. Ryder, J. Delano, C. Pieters, G. Lofgren, Lunar rocks, in *Lunar Source Book* (Cambridge Univ. Press, 1991), pp. 183–284.
2. B. Hapke, Space weathering from Mercury to the asteroid belt. *J. Geophys. Res. Planets* **106**, 10039–10073 (2001).
3. M. Abdel-Gawad, M. Blander, R. W. Grant, R. M. Housley, A. H. Muir Jr., Mössbauer spectroscopy of Apollo 11 samples, in *Apollo 11 Lunar Science Conference* (Pergamon Press, Inc., 1970), pp. 2251–2268.
4. F. H. Cocks, P. A. Klenk, S. A. Watkins, W. N. Simmons, J. C. Cocks, E. E. Cocks, J. C. Sussingham, Lunar ice: Adsorbed water on subsurface polar dust. *Icarus* **160**, 386–397 (2002).
5. J. D. Stopar, B. L. Jolliff, E. J. Speyerer, E. I. Asphaug, M. S. Robinson, Potential impact-induced water-solid reactions on the Moon. *Planet. Space Sci.* **162**, 157–169 (2018).
6. M. S. Thompson, T. J. Zega, P. Becerra, J. T. Keane, S. Byrne, The oxidation state of nanophase Fe particles in lunar soil: Implications for space weathering. *Meteorit. Planet. Sci.* **51**, 1082–1095 (2016).
7. K. Terada, S. Yokota, Y. Saito, N. Kitamura, K. Asamura, M. N. Nishino, Biogenic oxygen from Earth transported to the Moon by a wind of magnetospheric ions. *Nat. Astron.* **1**, 0026 (2017).
8. F. Vilas, K. S. Jarvis, M. J. Gaffey, Iron alteration minerals in the visible and near-infrared spectra of low-albedo asteroids. *Icarus* **109**, 274–283 (1994).
9. T. Hiroi, F. Vilas, J. M. Sunshine, Discovery and analysis of minor absorption bands in S-asteroid visible reflectance spectra. *Icarus* **119**, 202–208 (1996).
10. L. A. Taylor, J. C. Burton, Experiments on the stability of FeOOH on the surface of the Moon. *Meteoritics* **11**, 225–230 (1976).
11. S. O. Agrell, M. G. Bown, P. Gay, J. V. P. Long, J. D. C. McConnell, " Gaethite" on the moon and possible existence of other oxidized and hydroxyl-bearing phases in lunar impactites. *Meteoritics* **6**, 247–248 (1971).
12. J. Jedwab, A. Herbosch, R. Wollast, G. Naessens, N. Van Geen-Peers, Search for magnetite in lunar rocks and fines. *Science* **167**, 618–619 (1970).
13. F. Vilas, E. A. Jensen, D. L. Domingue, L. A. McFadden, C. J. Runyon, W. W. Mendell, A newly-identified spectral reflectance signature near the lunar South pole and the South Pole-Aitken Basin. *Earth Planets Space* **60**, 67–74 (2008).
14. R. O. Green, C. Pieters, P. Mouroulis, M. Eastwood, J. Boardman, T. Glavich, P. Isaacson, M. Annadurai, S. Besse, D. Barr, B. Buratti, D. Cate, A. Chatterjee, R. Clark, L. Cheek, J. Combe, D. Dhingra, V. Essandoh, S. Geier, J. N. Goswami, R. Green, V. Haemmerle, J. Head, L. Hovland, S. Hyman, R. Klima, T. Koch, G. Kramer, A. S. K. Kumar, K. Lee, S. Lundeen, E. Malaret, T. McCord, S. McLaughlin, J. Mustard, J. Nettles, N. Petro, K. Plourde, C. Racho, J. Rodriquez, C. Runyon, G. Sellar, C. Smith, H. Sobel, M. Staid, J. Sunshine, L. Taylor, K. Thaisen, S. Tompkins, H. Tseng, G. Vane, P. Varanasi, M. White, D. Wilson, The Moon Mineralogy Mapper (M^3) imaging spectrometer for lunar science: Instrument description, calibration, on-orbit measurements, science data calibration and on-orbit validation. *J. Geophys. Res* **116**, E00G19 (2011).
15. S. Li, R. E. Milliken, An empirical thermal correction model for Moon Mineralogy Mapper data constrained by laboratory spectra and Diviner temperatures. *J. Geophys. Res.* **121**, 2081–2107 (2016).
16. R. V. Morris, H. V. Lauer Jr., C. A. Lawson, E. K. Gibson Jr., G. A. Nace, C. Stewart, Spectral and other physicochemical properties of submicron powders of hematite (α-Fe2O3), maghemite (γ-Fe2O3), magnetite (Fe3O4), goethite (α-FeOOH), and lepidocrocite (γ-FeOOH). *J. Geophys. Res.* **90**, 3126–3144 (1985).
17. S. Lundeen, S. McLaughlin, R. Alanis, Moon Mineralogy Mapper Data Product Software Interface Specification, Version 9.10 (2011).
18. C. M. Pieters, E. M. Fischer, O. Rode, A. Basu, Optical effects of space weathering: The role of the finest fraction. *J. Geophys. Res. Planets* **98**, 20817–20824 (1993).
19. R. V. Morris, D. G. Agresti, H. V. Lauer Jr., J. A. Newcomb, T. D. Shelfer, A. V. Murali, Evidence for pigmentary hematite on Mars based on optical, magnetic, and Mossbauer studies of superparamagnetic (nanocrystalline) hematite. *J. Geophys. Res. Solid Earth* **94**, 2760–2778 (1989).
20. T. F. Bristow, D. L. Bish, D. T. Vaniman, R. V. Morris, D. F. Blake, J. P. Grotzinger, E. B. Rampe, J. A. Crisp, C. N. Achilles, D. W. Ming, B. L. Ehlmann, P. L. King, J. C. Bridges, J. L. Eigenbrode, D. Y. Sumner, S. J. Chipera, J. M. Moorokian, A. H. Treiman, S. M. Morrison, R. T. Downs, J. D. Farmer, D. D. Marais, P. Sarrazin, M. M. Floyd, M. A. Mischna, A. C. McAdam, The origin and implications of clay minerals from Yellowknife Bay, Gale crater Mars. *Am. Mineral.* **100**, 824–836 (2015).
21. R. V. Morris, D. C. Golden, Goldenrod pigments and the occurrence of hematite and possibly goethite in the Olympus–Amazonis region of Mars. *Icarus* **134**, 1–10 (1998).
22. B. Hapke, Bidirectional reflectance spectroscopy: 1. Theory. *J. Geophys. Res.* **86**, 3039–3054 (1981).
23. J. M. Sunshine, T. L. Farnham, L. M. Feaga, O. Groussin, F. Merlin, R. E. Milliken, M. F. A'Hearn, Temporal and spatial variability of lunar hydration as observed by the deep impact spacecraft. *Science* **326**, 565–568 (2009).
24. C. M. Pieters, J. N. Goswami, R. N. Clark, M. Annadurai, J. Boardman, B. Buratti, J.-P. Combe, M. D. Dyar, R. Green, J. W. Head, C. Hibbitts, M. Hicks, P. Isaacson, R. Klima, G. Kramer, S. Kumar, E. Livo, S. Lundeen, E. Malaret, T. McCord, J. Mustard, J. Nettles, N. Petro, C. Runyon, M. Staid, J. Sunshine, L. A. Taylor, S. Tompkins, P. Varanasi, Character and Spatial Distribution of OH/H_2O on the Surface of the Moon Seen by M^3 on Chandrayaan-1. *Science* **326**, 568–572 (2009).
25. R. N. Clark, Detection of adsorbed water and hydroxyl on the Moon. *Science* **326**, 562–564 (2009).
26. B. M. Jones, A. Aleksandrov, K. Hibbitts, M. D. Dyar, T. M. Orlando, Solar wind-induced water cycle on the Moon. *Geophys. Res. Lett.* **45**, 10,959–910,967 (2018).
27. R. T. Daly, P. H. Schultz, The delivery of water by impacts from planetary accretion to present. *Sci. Adv.* **4**, eaar2632 (2018).
28. R. J. Williams, E. K. Gibson, The origin and stability of lunar goethite, hematite and magnetite. *Earth Planet. Sci. Lett.* **17**, 84–88 (1972).
29. A. R. Poppe, M. O. Fillingim, J. S. Halekas, J. Raeder, V. Angelopoulos, ARTEMIS observations of terrestrial ionospheric molecular ion outflow at the Moon. *Geophys. Res. Lett.* **43**, 6749–6758 (2016).
30. P. Bochsler, Solar wind ion composition. *Physica Scripta* **1987**, 55 (1987).
31. A. R. Poppe, W. M. Farrell, J. S. Halekas, Formation timescales of amorphous rims on lunar grains derived from ARTEMIS observations. *J. Geophys. Res. Planets* **123**, 37–46 (2018).
32. V. Peroomian, M. El-Alaoui, P. C. S. Brandt, The ion population of the magnetotail during the 17 April 2002 magnetic storm: Large-scale kinetic simulations and IMAGE/HENA observations. *J. Geophys. Res. Space Phys.* **116**, A05214 (2011).
33. S. A. Stern, The lunar atmosphere: History, status, current problems, and context. *Rev. Geophys.* **37**, 453–491 (1999).
34. U. Mall, E. Kirsch, K. Cierpka, B. Wilken, A. Söding, F. Neubauer, G. Gloeckler, A. Galvin, Direct observation of lunar pick-up ions near the Moon. *Geophys. Res. Lett.* **25**, 3799–3802 (1998).
35. A. R. Poppe, J. S. Halekas, M. Sarantos, G. T. Delory, The self-sputtered contribution to the lunar exosphere. *J. Geophys. Res. Planets* **118**, 1934–1944 (2013).
36. C. Wöhler, A. Grumpe, A. A. Berezhnoy, V. V. Shevchenko, Time-of-day–dependent global distribution of lunar surficial water/hydroxyl. *Sci. Adv.* **3**, e1701286 (2017).
37. S. Li, R. E. Milliken, Water on the surface of the Moon as seen by the Moon Mineralogy Mapper: Distribution, abundance, and origins. *Sci. Adv.* **3**, e1701471 (2017).
38. M. Adams, P. Schultz, S. Sugita, J. Goguen, in *Lunar and Planetary Science Conference* (1997), vol. 28, pp. 3.
39. M. Lemelin (University of Hawaii at Manoa, Honolulu, 2016).

Downloaded from http://advances.sciencemag.org/ on September 14, 2020

40. J. R. Szalay, P. Pokorný, Z. Sternovsky, Z. Kupihar, A. R. Poppe, M. Horányi, Impact ejecta and gardening in the lunar polar regions. *J. Geophys. Res. Planets* **124**, 143–154 (2019).
41. M. Horányi, J. R. Szalay, S. Kempf, J. Schmidt, E. Grün, R. Srama, Z. Sternovsky, A permanent, asymmetric dust cloud around the Moon. *Nature* **522**, 324–326 (2015).
42. S. K. Noble, L. P. Keller, C. M. Pieters, Evidence of space weathering in regolith breccias II: Asteroidal regolith breccias. *Meteorit. Planet. Sci.* **45**, 2007–2015 (2010).
43. W. F. Buckingham, S. E. Sommer, Mineralogical characterization of rock surfaces formed by hydrothermal alteration and weathering; application to remote sensing. *Econ. Geol.* **78**, 664–674 (1983).
44. R. V. Morris, D. G. Schulze, H. V. Lauer Jr., D. G. Agresti, T. D. Shelfer, Reflectivity (visible and near IR), Mössbauer, static magnetic, and X ray diffraction properties of aluminum-substituted hematites. *J. Geophys. Res. Planets* **97**, 10257–10266 (1992).
45. K. Hashizume, M. Chaussidon, Two oxygen isotopic components with extra-selenial origins observed among lunar metallic grains–In search for the solar wind component. *Geochim. Cosmochim. Acta* **73**, 3038–3054 (2009).
46. S. Besse, J. Sunshine, M. Staid, J. Boardman, C. Pieters, P. Guasqui, E. Malaret, S. McLaughlin, Y. Yokota, J.-Y. Li, A visible and near-infrared photometric correction for Moon Mineralogy Mapper (M^3). *Icarus* **222**, 229–242 (2013).
47. S. Li, L. Li, Radiative transfer modeling for quantifying lunar surface minerals, particle size, and submicroscopic metallic Fe. *J. Geophys. Res. Planets* **116**, E09001 (2011).
48. S. Li, R. E. Milliken, Estimating the modal mineralogy of eucrite and diogenite meteorites using visible–near infrared reflectance spectroscopy. *Meteorit. Planet. Sci.* **50**, 1821–1850 (2015).
49. Y. G. Shkuratov, Y. S. Grynko, Light scattering by media composed of semitransparent particles of different shapes in ray optics approximation: Consequences for spectroscopy, photometry, and polarimetry of planetary regoliths. *Icarus* **173**, 16–28 (2005).
50. K. M. Robertson, R. E. Milliken, S. Li, Estimating mineral abundances of clay and gypsum mixtures using radiative transfer models applied to visible-near infrared reflectance spectra. *Icarus* **277**, 171–186 (2016).
51. P. G. Lucey, Model near-infrared optical constants of olivine and pyroxene as a function of iron content. *J. Geophys. Res. Planets* **103**, 1703–1713 (1998).
52. J. T. S. Cahill, D. T. Blewett, N. V. Nguyen, K. Xu, O. A. Kirillov, S. J. Lawrence, B. W. Denevi, E. I. Coman, Determination of iron metal optical constants: Implications for ultraviolet, visible, and near-infrared remote sensing of airless bodies. *Geophys. Res. Lett.* **39**, L10204 (2012).
53. D. A. Leich, T. A. Tombrello, A technique for measuring hydrogen concentration versus depth in solid samples. *Nucl. Instrum. Meth.* **108**, 67–71 (1973).
54. Y. Shkuratov, L. Starukhina, H. Hoffmann, G. Arnold, A model of spectral albedo of particulate surfaces: Implications for optical properties of the Moon. *Icarus* **137**, 235–246 (1999).
55. J. Mitchell et al., in *Lunar and Planetary Science Conference Proceedings* (1972), vol. 3, pp. 3235.
56. J. F. Vedder, Craters formed in mineral dust by hypervelocity microparticles. *J. Geophys. Res.* **77**, 4304–4309 (1972).
57. D. M. Hurley, M. Benna, Simulations of lunar exospheric water events from meteoroid impacts. *Planet. Space Sci.* **162**, 148–156 (2018).
58. H. E. Newsom, Hydrothermal alteration of impact melt sheets with implications for Mars. *Icarus* **44**, 207–216 (1980).
59. P. Eberhardt, J. Geiss, H. Graf, N. Grögler, U. Krähenbühl, H. Schwaller, J. Schwarzmüller, A. Stettler, Trapped solar wind noble gases, exposure age and K/Ar-age in Apollo 11 lunar fine material. *Science* **167**, 558–560 (1970).
60. C. K. Sim, S. S. Kim, P. G. Lucey, I. Garrick-Bethell, Y. J. Choi, Asymmetric space weathering on lunar crater walls. *Geophys. Res. Lett.* **44**, 11,273–211,281 (2017).
61. J. R. Szalay, M. Horányi, Annual variation and synodic modulation of the sporadic meteoroid flux to the Moon. *Geophys. Res. Lett.* **42**, 10,580–510,584 (2015).
62. R. L. Klima, M. D. Dyar, C. M. Pieters, Near-infrared spectra of clinopyroxenes: Effects of calcium content and crystal structure. *Meteorit. Planet. Sci.* **46**, 379–395 (2011).
63. P. J. Isaacson, A. B. Sarbadhikari, C. M. Pieters, R. L. Klima, T. Hiroi, Y. Liu, L. A. Taylor, The lunar rock and mineral characterization consortium: Deconstruction and integrated mineralogical, petrologic, and spectroscopic analyses of mare basalts. *Meteorit. Planet. Sci.* **46**, 228–251 (2011).
64. M. Querry, Optical Constants, contractor report, in *US Army Chemical Research, Development and Engineering Center (CRDC), Aberdeen Proving Ground, MD* (1985), vol. 418.

Acknowledgments

Funding: S.L. acknowledges that a portion of this work is supported by the NASA Lunar Data Analysis grant 80NSSC19K0369. A.A.F. and V.Z.S. acknowledge that a portion of this research was carried out at the Jet Propulsion Laboratory, California Institute of Technology, under a contract with the NASA. A.R.P. acknowledges support from the NASA SSERVI institute via the DREAM2 team, grant no. NNX14AG16A. **Author contributions:** S.L. conceived the project and conducted the study; A.A.F., P.G.L., A.R.P., V.Z.S., D.M.H., and P.H.S. contributed to data analysis; S.L. wrote the manuscript; all coauthors read, commented, and agreed on the submitted manuscript. **Competing interests:** The authors declare that they have no competing interests. **Data and materials availability:** The Moon Mineralogy Mapper L1B data are available at https://pds-imaging.jpl.nasa.gov/volumes/m3.html; the azimuth angle data are available at http://imbrium.mit.edu/BROWSE/SLDEM2015_AZIMUTH/TILES/; the surface slope data are downloaded from http://imbrium.mit.edu/BROWSE/SLDEM2015_SLOPE/TILES/; the laboratory spectral data are from the RELAB database at Brown University www.planetary.brown.edu/relabdocs/relab_disclaimer.htm and the spectral database at USGS https://crustal.usgs.gov/speclab/QueryAll07a.php.

Submitted 12 November 2019
Accepted 17 July 2020
Published 2 September 2020
10.1126/sciadv.aba1940

Citation: S. Li, P. G. Lucey, A. A. Fraeman, A. R. Poppe, V. Z. Sun, D. M. Hurley, P. H. Schultz, Widespread hematite at high latitudes of the Moon. *Sci. Adv.* **6**, eaba1940 (2020).

Downloaded from http://advances.sciencemag.org/ on September 14, 2020

Science Advances

Widespread hematite at high latitudes of the Moon

Shuai Li, Paul G. Lucey, Abigail A. Fraeman, Andrew R. Poppe, Vivian Z. Sun, Dana M. Hurley and Peter H. Schultz

Sci Adv **6** (36), eaba1940.
DOI: 10.1126/sciadv.aba1940

ARTICLE TOOLS http://advances.sciencemag.org/content/6/36/eaba1940

SUPPLEMENTARY MATERIALS http://advances.sciencemag.org/content/suppl/2020/08/31/6.36.eaba1940.DC1

REFERENCES This article cites 57 articles, 10 of which you can access for free
http://advances.sciencemag.org/content/6/36/eaba1940#BIBL

PERMISSIONS http://www.sciencemag.org/help/reprints-and-permissions

Use of this article is subject to the Terms of Service

Science Advances (ISSN 2375-2548) is published by the American Association for the Advancement of Science, 1200 New York Avenue NW, Washington, DC 20005. The title *Science Advances* is a registered trademark of AAAS.

Copyright © 2020 The Authors, some rights reserved; exclusive licensee American Association for the Advancement of Science. No claim to original U.S. Government Works. Distributed under a Creative Commons Attribution NonCommercial License 4.0 (CC BY-NC).

Downloaded from http://advances.sciencemag.org/ on September 14, 2020